

A force correction scheme for a volume-filtered formulation of flow over a permeable particle bed

By D. Fust, S. V. Apte[†], AND S. Balachandar[‡]

Pore-resolved direct numerical simulations (PR-DNS) of open-channel flow over a porous bed composed of randomly packed, monodispersed, spherical particles are performed for a range of porosities and Reynolds numbers. The resultant data are explicitly filtered using three filter kernels and compared against existing drag force closure models based on Darcy-Forchheimer parameterizations. A methodology is developed for a variable filter width that more accurately captures the interface and free-stream regions without introducing any nonphysical oscillations in porosity or permeability. Finally, a physically informed correction scheme for classic permeability models is devised to improve the accuracy of drag force predictions in the interface region.

1. Introduction

Flow over and through permeable surfaces is commonly encountered in a wide range of problems, for example, flows in an oil well bore that are surrounded by a porous formation, stream or river flow over gravel beds, and atmospheric flow over plant canopies, or densely built-up urban areas. Retention and transport of chemicals, pollutants, nutrients, dissolved oxygen, or heat between the surface water and groundwater in river and stream flows over a porous bed of particles are critical for stream ecology and have enormous societal value in predicting sources of fresh drinking water, nutrient cycling, and sustaining diverse aquatic ecosystems (Hester *et al.* 2017). Turbulent transport across the sediment-water interface (SWI), coherent flow structures, and non-Darcy flow within the sediment bed have been hypothesized as critical mechanisms impacting this transport. The permeability Reynolds number, representing the ratio between the permeability scale and the viscous scale, $Re_K = \sqrt{K}/(\nu/u_\tau)$, is typically used to identify different flow regimes based on the dominant transport mechanism across the SWI. Turbulence is dominant near the SWI and can penetrate within the sediment bed for $Re_K > 1$. Recent pore-resolved simulations by Karra *et al.* (2023) for $Re_K \sim \mathcal{O}(1-10)$ have shown that bed permeability increases friction coefficient, reduces the wall-blocking effect present in impermeable walls, and reduces near-bed anisotropy in turbulence intensities.

To study such flows on practical scales, reduced-order homogenized modeling approaches based on volume-averaged governing equations, requiring fewer computational resources, have been developed to obtain a continuum model for the superficial velocity through the porous bed (Whitaker 1996). In this approach, the averaged equations are derived by applying the method of volume averaging over a representative filter volume. This gives rise to additional terms that need closure models. For example, the momentum exchange between the fluid and the particle bed needs a model for the drag force. The approach splits the domain into a homogeneous free stream with unit porosity ($\varepsilon_\gamma = 1$)

[†] School of Mechanical, Industrial and Manufacturing Engineering, Oregon State University

[‡] Department of Mechanical and Aerospace Engineering, University of Florida

and a homogeneous porous region with a porosity equal to the particle packing ($\varepsilon_\gamma = \varepsilon_c$). The interfacial boundary between the porous region and the free stream in a typical two-domain approach is treated by ensuring continuity of flow variables while prescribing a stress jump condition at the interface (Ochoa-Tapia & Whitaker 1995*b,a*; Rosti *et al.* 2015) with coefficients calibrated using experimental data.

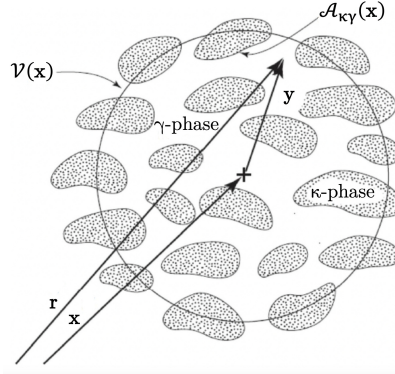
For a randomly packed bed of particles, defining a sharp interface between the homogeneous free-stream and homogeneous porous region is not straightforward owing to local protrusions of the top layer of particles into the bed. An alternative single-domain approach treats the composite interface region as a continuum with smooth variation of the porosity and permeability across the two regions (Breugem *et al.* 2006; Pokrajac & De Lemos 2015). Application of such a single-domain, variable-porosity model for turbulent flows requires disparate filtering volumes for the free-stream region and the porous region. To capture the rapid bed-normal variations in the fluid flow variables in the turbulent free stream, a filter based on the computational grid with thin, bed-parallel volumes is used in typical wall-resolved, large-eddy simulations of channel flows with near-wall grid resolution of $y^+ \sim 1$. In contrast, the representative averaging volume within the porous bed is typically much larger and scales with the particle size, which in wall units can be $\mathcal{O}(10)$ for stream flows. Pokrajac & De Lemos (2015) developed the volume-averaging equations by allowing the filtering volume to vary in space, especially in the bed-normal direction to address this disparity in scales.

This work focuses on the fundamental questions related to this single-domain, diffuse-interface, variable-porosity approach: (i) How should the filter width be chosen and varied in the interface region, and what is its effect on the drag force closure? (ii) Are the standard drag closure, such as the Ergun model, designed on the basis of uniform porosity, applicable in the interface region of variable porosity? (iii) How can the force closure in the interface region be improved? To address these questions, pore-resolved simulations of flow over a randomly packed bed of particles are conducted using a verified and validated fictitious domain approach as done by Apte *et al.* (2009) and Karra *et al.* (2023). The pore-resolved data are explicitly filtered using different filter kernels and filter widths to evaluate the standard drag closure and develop an improved model.

The rest of the report is arranged as follows. In Section 2, the method of volume-averaging and the volume-filtered equations are described. Explicit filtering of the data to evaluate existing drag closures and to devise a correction scheme is discussed in Section 3, followed by conclusions in Section 4.

2. Mathematical formulation

Figure 1 shows a schematic of a representative elementary volume (REV) over which averaging is performed to derive the volume-filtered Navier-Stokes equations (Whitaker 1996). Here, γ represents the fluid phase, κ represents the solid phase, $\mathcal{A}_{\gamma\kappa}(\mathbf{x})$ represents the surface area between the κ and γ phases, and $\mathcal{V}(\mathbf{x})$ is the averaging domain encompassing the fluid and solid phases, where \mathbf{x} is its centroid. To obtain meaningful filtered equations, it is assumed that the equivalent length scale associated with the pore size is much smaller than the length scale associated with the REV, which in turn is much smaller than the global length scale of the porous medium. In addition, variations in porosity averaged over the REV are assumed negligible. The volume-averaging operator is represented as $\langle \cdot \rangle$ and, when applied to any quantity ψ in the fluid phase, gives the


 FIGURE 1. Averaging volume over the solid (κ) and the fluid (γ) phase (Whitaker 1996).

superficial average,

$$\langle \psi_\gamma \rangle = \frac{1}{V} \int_{\mathbf{r} \in \mathcal{V}(\mathbf{x})} \mathcal{G}(\mathbf{y}) I_\gamma(\mathbf{r}) \psi(\mathbf{r}) d\mathcal{V}(\mathbf{r}); \quad I_\gamma(\mathbf{r}) = \begin{cases} 1, & \mathbf{r} \in \mathcal{V}_\gamma, \\ 0, & \mathbf{r} \in \mathcal{V}_\kappa, \end{cases} \quad (2.1)$$

where \mathcal{V} is the total volume in the averaging domain, $I_\gamma(\mathbf{r})$ is the indicator function, and $\mathcal{G}(\mathbf{y})$ is the filter function applied around the center of the averaging volume (\mathbf{x}) subject to the normalization condition, $\int_{\mathbf{r} \in \mathcal{V}(\mathbf{x})} \mathcal{G}(\mathbf{y}) d\mathcal{V} = 1$. The intrinsic average is defined using the averaging volume of the fluid phase (\mathcal{V}_γ),

$$\langle \psi_\gamma \rangle^\gamma = \frac{1}{V_\gamma} \int_{\mathbf{r} \in \mathcal{V}(\mathbf{x})} \mathcal{G}(\mathbf{y}) I_\gamma(\mathbf{r}) \psi(\mathbf{r}) d\mathcal{V}(\mathbf{r}). \quad (2.2)$$

As a result, the superficial averaged quantity $\langle \psi_\gamma \rangle$ can be related to the intrinsic averaged quantity as $\langle \psi_\gamma \rangle = \varepsilon_\gamma \langle \psi_\gamma \rangle^\gamma$, where ε_γ is the porosity of the medium, obtained from Eq. (2.1) with $\psi(\mathbf{r}) = 1$.

The volume-averaged continuum equations for a stationary porous medium with spatial variations in porosities are (Whitaker 1996)

$$\begin{aligned} \rho_\gamma \frac{\partial \varepsilon_\gamma \langle \mathbf{u}_\gamma \rangle^\gamma}{\partial t} + \rho_\gamma \nabla \cdot [\varepsilon_\gamma \langle \mathbf{u}_\gamma^\gamma \rangle \otimes \langle \mathbf{u}_\gamma^\gamma \rangle] &= -\varepsilon_\gamma \nabla \langle p_\gamma \rangle^\gamma + \rho_\gamma \varepsilon_\gamma \mathbf{f}_b + \mu_\gamma \nabla \cdot [\varepsilon_\gamma \nabla \otimes \langle \mathbf{u}_\gamma \rangle^\gamma] + \\ \mu_\gamma \langle \mathbf{u}_\gamma \rangle^\gamma \nabla^2 \varepsilon_\gamma + \underbrace{\frac{1}{V} \int_{\mathcal{A}_{\gamma\kappa}} \mathcal{G}(\mathbf{y}) \mathbf{n}_{\gamma\kappa} \cdot (-\mathbf{I} \tilde{p}_\gamma + \mu_\gamma \nabla \otimes \tilde{\mathbf{u}}_\gamma) d\mathcal{A}}_{\text{surface-filter closure}} &- \underbrace{\rho_\gamma \nabla \cdot [\varepsilon_\gamma \langle \tilde{\mathbf{u}}_\gamma \otimes \tilde{\mathbf{u}}_\gamma \rangle]}_{\text{volume-filter closure}}. \end{aligned} \quad (2.3)$$

Here, ρ_γ is the fluid density, μ_γ is the dynamic viscosity, and \mathbf{f}_b is the body force per unit volume due to an external pressure gradient. The surface- and volume-filter closure terms need to be modeled. The volume-filter term is the subfilter-scale stress similar to the subgrid-scale stress in large-eddy simulations and can be modeled using standard models such as the dynamic Smagorinsky model (Germano *et al.* 1991). The surface-filter closure term represents the net drag force on the interfacial area $\mathcal{A}_{\gamma\kappa}$ between the γ and κ phases, where $\mathbf{n}_{\gamma\kappa}$ is the unit normal vector pointing from the κ phase to the γ phase. The drag force is based on the spatial fluctuations in velocity and pressure defined as

$$\tilde{\mathbf{u}}_\gamma = \mathbf{u}_\gamma - \langle \mathbf{u}_\gamma \rangle^\gamma, \quad \tilde{p}_\gamma = p_\gamma - \langle p_\gamma \rangle^\gamma. \quad (2.4)$$

As shown by Whitaker (1996) using theoretical analysis, the surface-filter term can be expressed in terms of an effective permeability,

$$\frac{1}{\mathcal{V}} \int_{\mathcal{A}_{\gamma\kappa}} \mathcal{G}(\mathbf{y}) \mathbf{n}_{\gamma\kappa} \cdot (-\mathbf{I}\tilde{p}_\gamma + \mu_\gamma \nabla \otimes \tilde{\mathbf{u}}_\gamma) \mathbf{d}\mathcal{A} = -\mu_\gamma \varepsilon_\gamma \underbrace{[\mathbf{K}^{-1}(\mathbf{I} + \mathbf{F})]}_{\mathbf{K}_{\text{eff}}^{-1}} \langle \mathbf{u}_\gamma \rangle, \quad (2.5)$$

where \mathbf{K} and \mathbf{F} are the permeability and Forchheimer tensors (Whitaker 1996; Breugem *et al.* 2006), respectively, \mathbf{K}_{eff} is the effective permeability tensor, and $\langle \mathbf{u}_\gamma \rangle$ is the superficial velocity.

To evaluate the right-hand side of Eq. (2.5), a model for the effective permeability is needed. In the limit of Stokes flow, the drag term depends only on the permeability tensor, whereas the inertial effects are important at higher pore Reynolds numbers when the Forchheimer correction becomes dominant. The permeability tensor depends mainly on the geometry of the porous medium, whereas the Forchheimer tensor can depend on the pore Reynolds number, the orientation of the pores relative to the direction of the volume-averaged flow and pressure gradient, and other geometric parameters. Universally valid expressions for these tensors have not been successfully developed. They are determined empirically through substantial experimental data and numerical simulations in the Stokes and steady or unsteady laminar regimes for uniform porosity. For flow fields through packed sediment beds, a widely used relation for the drag force is the Ergun-type equation with empirically obtained coefficients in permeability and Forchheimer tensors (Macdonald *et al.* 1979),

$$\mathbf{K} = \frac{d_p^2 \varepsilon_\gamma^3}{A(1 - \varepsilon_\gamma)^2} \mathbf{I}, \quad \mathbf{F} = \frac{\varepsilon_\gamma}{B(1 - \varepsilon_\gamma)} \frac{\rho_\gamma d_p |\langle \mathbf{u}_\gamma \rangle^\gamma|}{\mu_\gamma} \mathbf{I}, \quad (2.6)$$

where $d_p = 6\mathcal{V}_\kappa/A_{\gamma\kappa}$ is the effective diameter of the solid beads, with \mathcal{V}_κ their volume and $\mathcal{A}_{\gamma\kappa}$ the surface area. Typically, $A = 180$ and $A/B = 1.0$ – 1.8 are used. Sadowski & di Mare (2023) conducted an analysis for flow over arranged packing of cubes and observed that the model coefficients need adjustments based on the configurations used. The coefficients are adjusted to match the pore-resolved permeability deep within the bed obtained from the filtered PR-DNS data to ensure that the Darcy velocity deep within the bed is accurately captured. The Forchheimer correction is small for the low Reynolds numbers considered. The left-hand side of Eq. (2.5) can be directly evaluated from explicit filtering of DNS data. Substituting for the fluctuations (Eq. (2.4)) and simplifying we obtain,

$$\frac{1}{\mathcal{V}} \int_{\mathcal{A}_{\gamma\kappa}} \mathcal{G}(\mathbf{y}) \mathbf{n}_{\gamma\kappa} \cdot (-\mathbf{I}\tilde{p}_\gamma + \mu_\gamma \nabla \otimes \tilde{\mathbf{u}}_\gamma) \mathbf{d}\mathcal{A} = \frac{1}{\mathcal{V}} \int_{\mathcal{A}_{\gamma\kappa}} \mathcal{G}(\mathbf{y}) \mathbf{n}_{\gamma\kappa} \cdot (-\mathbf{I}p_\gamma + \mu_\gamma \nabla \otimes \mathbf{u}_\gamma) \mathbf{d}\mathcal{A} - \langle p \rangle^\gamma \nabla \varepsilon_\gamma + \mu_\gamma \nabla \varepsilon_\gamma \cdot \nabla \otimes \langle \mathbf{u}_\gamma \rangle^\gamma. \quad (2.7)$$

Here, the second-term on the right-hand side is the rigidity constraint force in the fictitious domain method. The last two terms can be computed from explicit filtering and can also be combined with the first and third terms on the right-hand side of Eq. (2.3).

3. Results

In order to explore the efficacy of the Darcy-Forchheimer drag parameterization, PR-DNS of open-channel flow over a bed of randomly packed, monodispersed, spherical par-

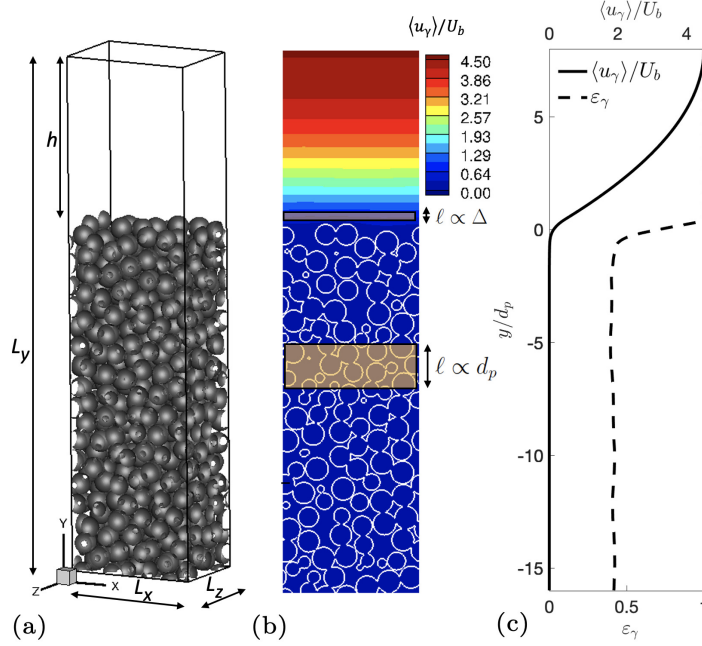


FIGURE 2. Schematic diagram for flow over a bed of randomly packed, monodispersed, spherical particles: (a) computational domain, (b) slice through the symmetry plane showing velocity magnitude contours and filter lengths within the bed and in the free stream, and (c) bed-normal variation of the porosity and superficial velocity using a variable cellular filter.

ticles are performed using a fictitious domain method (Apte *et al.* 2009) at bed porosities of $\varepsilon_c = 0.41, 0.50, 0.60,$ and 0.70 and bulk Reynolds numbers $Re = \rho_\gamma U_b h / \mu_\gamma$ of 4, 50, and 500. The bulk Reynolds number is based on the free-stream channel height h and bulk velocity U_b computed by integrating over the entire domain including free-stream and bed regions. The computational domain, shown in Figure 2(a), is doubly periodic in the streamwise (x) and spanwise (z) directions with lengths $L_x = 6d_p$, $L_y = 24d_p$, and $L_z = 4d_p$. The free-stream height is $8d_p$, and the wall-normal coordinate extends from $-16d_p$ to $8d_p$, where the roughness crest extends to a maximum of $y = 0.5d_p$, owing to protrusions of particles caused by random packing. A uniform, cubic grid resolution of $192 \times 768 \times 128$ is used in all cases, yielding approximately 32 grid points per particle diameter. Flow is driven by a pressure gradient obtained based on a constant, target mass flow rate, while slip conditions are imposed at the top surface and underneath the porous bed. Figure 2(b) shows contours of the velocity magnitude in the symmetry plane together with different filtering length scales within the bed and in the free stream. Figure 2(c) shows bed-normal variations in the porosity and superficial velocity obtained from filtered DNS data using the cellular filter described below.

For sufficiently low Reynolds numbers, the inertial terms in the volume-averaged momentum equation are negligible, and the x component of the inverse permeability is $K^{-1} = \tilde{f}_d / (\mu_\gamma \varepsilon_\gamma \langle u_\gamma \rangle)$, where \tilde{f}_d is the subfilter drag force in the x direction, directly computed from Eq. (2.7) using the DNS data. For the present configuration, a rectangular prism made up of the entire lengths (L_x and L_z) in the homogeneous directions and variable thickness 2ℓ in the vertical direction is used. Three different filter kernels [see Figure 3(a)], namely, box ($\mathcal{G}_B(y)$), cellular ($\mathcal{G}_C(y)$), and Gaussian ($\mathcal{G}_G(y)$), are used with

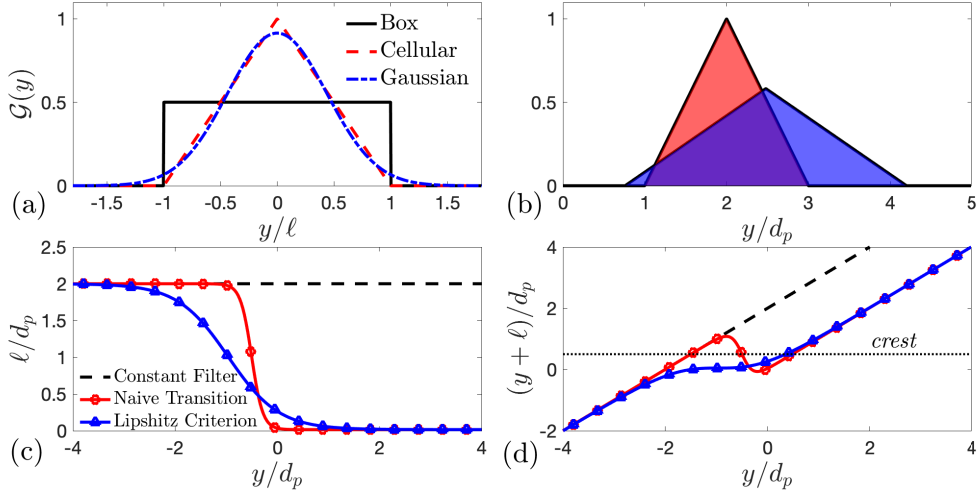


FIGURE 3. (a) Different filter kernels corresponding to a fixed filter width, ℓ . (b) Overlapping behavior of variable-length cellular filters that do not meet the Lipschitz criterion. (c) Cellular kernel transitions in the interface region showing filter centroid location versus filter width for a constant filter, variable filter with naive transition not satisfying the Lipschitz criterion, and Lipschitz criterion filter. (d) Filter centroid location versus upper limit of filtering volume, with the superimposed roughness crest denoted by the dotted line.

a normalization condition enforced numerically,

$$\mathcal{G}_B(y) = \begin{cases} \frac{\ell}{2} & |y| < \ell \\ 0 & \text{otherwise} \end{cases}, \quad \mathcal{G}_C(y) = \begin{cases} \frac{\ell - |y|}{\ell} & |y| < \ell \\ 0 & \text{otherwise} \end{cases}, \quad (3.1a)$$

$$\mathcal{G}_G(y) = \begin{cases} \frac{1}{\sqrt{2\pi\sigma^2}} \exp\left(-\frac{y^2}{2\sigma^2}\right) & |y| < n\sigma \\ 0 & \text{otherwise} \end{cases}. \quad (3.1c)$$

The tails of the noncompact, Gaussian kernel are clipped after $n = 5$ with $\sigma = 0.4366\ell$ to minimize the L_2 error between the Gaussian and cellular/box kernels. For each kernel, the filter width (ℓ) should be large enough to form a REV that sufficiently smooths inhomogeneities within the particle bed. In the homogeneous porous region, the filter width is proportional to $d_p^+ \sim \mathcal{O}(10)$, whereas in the homogeneous fluid region, it is proportional to the grid size with $\Delta^+ \sim 1$ in the near-wall region. Therefore, in order to preserve the fidelity of the large-eddy simulation in the near-wall fluid region, the filter width must transition in size in the interface region, which is accomplished using a hyperbolic tangent function,

$$\ell(y) = \frac{1}{2}(\ell_p + \ell_f) - \frac{\ell_p - \ell_f}{2} \tanh\left(\frac{\alpha(y - y_0)}{s}\right), \quad (3.2)$$

where $\ell_p \propto d_p$ is the target filter width in the homogeneous porous region, $\ell_f \propto \Delta$ is the target filter width in the free-stream region, s is a length scale related to the size of REV, α is a unitless parameter controlling the rate of transition in filter width, and y_0 is the transition offset. If the filter width is changed too rapidly such that the two adjacent filtering volumes overlap as in Figure 3(b), nonphysical oscillations can occur in the filtered quantities. To avoid such nonphysical oscillations, the filter width transition

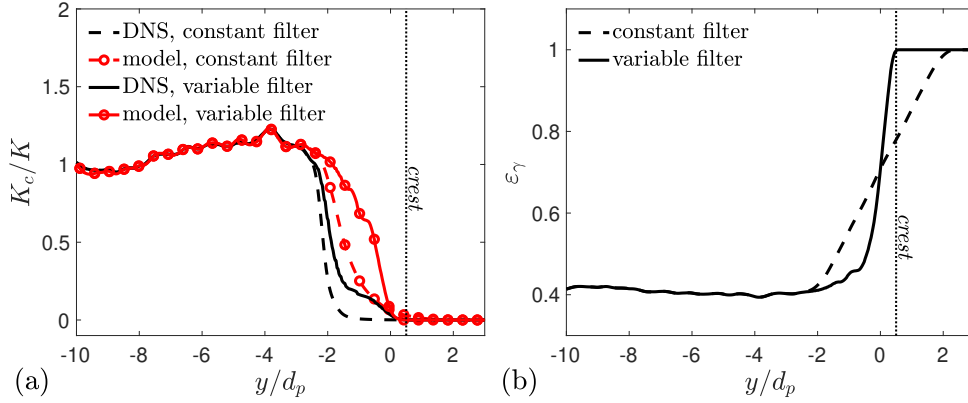


FIGURE 4. Bed-normal variations of (a) porosity and (b) inverse permeability normalized by its value within the bed (K_c^{-1}) for constant and variable filter widths using a cellular filter. Filtered permeability is compared with that predicted by the model (Eq. 2.6).

should satisfy the Lipschitz criterion,

$$|\ell(y_2) - \ell(y_1)| \leq k|y_2 - y_1|, \quad k = 1; \quad \text{or} \quad \sup_{y \in \Omega} \left| \frac{d\ell}{dy} \right| \leq 1, \quad (3.3)$$

where Ω is the computational domain. This requires that $\alpha/s \leq 2/(\ell_p - \ell_f)$ for the box filter and cellular filters, whereas for the clipped Gaussian filter, $\alpha/s \leq 2/[(n\sigma/\ell)(\ell_p - \ell_f)]$, where the factor $n\sigma/\ell$ accounts for the support extending beyond a radius ℓ of the filter's origin. This suggests that filter length may transition more rapidly for compact filters without the Lipschitz condition, although the oscillations induced by filter overlapping may be less severe for filter kernels with rapidly decaying tails.

Figure 3(c) compares the filter width in the interface region for constant and variable filter widths with (i) naive transition, where the filter width is changed too rapidly, and (ii) transition following the Lipschitz criterion. With the naive transition, the edges of the filtering volume encounter the roughness crest multiple times when convolved in the bed-normal direction, as shown by the hump in Figure 3(d). Such a rapid transition artificially induces peaks and oscillations in filtered quantities in the interface region, which have been observed with cellular filters applied to arranged packing of cubes (Breugem 2005; Sadowski & di Mare 2023). In contrast, a transition satisfying the Lipschitz criterion avoids the overlap and eliminates the hump, as shown in Figure 3(d), and any resultant nonphysical oscillations in filtered quantities.

Figure 4(a,b) compares the bed-normal variations of porosity and normalized inverse permeability obtained using the filtered DNS data with constant and variable filter widths for a cellular filter. The filter width within the bed was chosen to be $\ell_p = 2d_p$, which was sufficiently large that the modeled and filtered permeability deep within the bed (K_c) coincide. The transition offset, y_0 , was computed on the basis of a transition rate, α/s , that satisfies the Lipschitz criterion, such that 95% of the filter length transition occurs beneath the roughness crest. Constant filter width gives a porosity variation that is highly diffused in the free stream, whereas the variable filter width shows a much sharper transition near the crest. The porosity profile shows small wiggles within the bed owing to the random arrangement of spheres. These small wiggles are amplified in the permeability distribution; however, they are consistent, as the model predictions

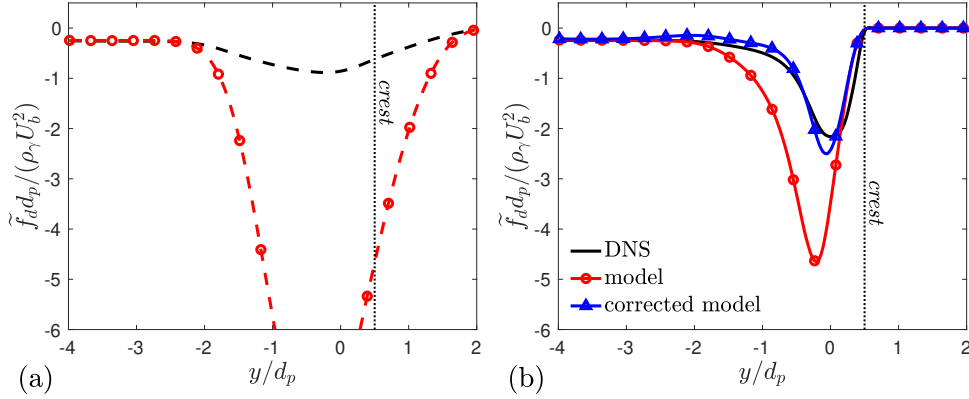


FIGURE 5. Comparison of bed-normal variation of normalized drag force for a bed packing of $\varepsilon_c = 0.41$ between the filtered DNS and the prediction by the permeability model for cellular filter: (a) constant filter width (dashed lines) of $\ell_p = 2d_p$ and (b) variable filter width (solid lines). The roughness crest location is indicated by a dotted line.

match well with the filtered DNS within the bed. In contrast, in the interface region, Figure 4(b) shows that the model predictions for inverse permeability are significantly higher in comparison to the filtered DNS data for both the constant and variable filter widths. Similar differences are observed with box and Gaussian filters.

Figure 5(a) shows the bed-normal drag variation for the model and filtered DNS using the cellular filter with constant filter width. The filtered drag force is significantly diffused owing to the large filter width in the interface region, and there is nonzero drag even in the free stream. The significant overprediction of the modeled drag force is attributed to (i) larger values of K^{-1} in the transition region and (ii) sampling of the faster free-stream velocity in computing the superficial velocity, $\langle u_\gamma \rangle$, needed to compute the force. The variable filter width, however, does not diffuse the drag force in the free stream, as shown in Figure 5(b). Since the porosity profile transitions sharply near the interface with variable filter width, the overprediction of the modeled force is significantly reduced. The high velocity values in the free stream are not sampled by the variable filter.

To further improve the drag prediction, a correction scheme is applied to the permeability value in the interface region. In the homogeneous porous region, inertial effects and porosity gradients vanish and the momentum equations, written in terms of the superficial velocity, reduce to the Brinkman equations involving balance between the axial pressure gradient (or the body force), viscous, and drag forces. The solution is an exponential velocity profile (Breugem *et al.* 2006) that decreases from the top of the homogeneous porous region to the Darcy velocity U_D deep within the bed that depends on the imposed pressure gradient, bed porosity (ε_c), and permeability (K_c). This exponential profile for the superficial velocity is assumed to be valid even in the interfacial region up to the crest and is modeled as

$$\frac{\langle u_\gamma \rangle^B}{U_D} = 1 + \left(\frac{U_I}{U_D} - 1 \right) \exp \left[\frac{a(y - y_I)}{\ell} \right], \quad (3.4)$$

where U_I is the velocity at the top of the interface region (near crest) at location y_I , U_D is the Darcy velocity deep within the bed, $\langle u_\gamma \rangle^B$ is the Brinkman velocity, and a/ℓ is the filter length scale that can be used as a tuning parameter. Direct simulations by Breugem *et al.* (2006) confirm that the Brinkman exponential velocity profile within

Re	ε_c	Box	Cellular	Gaussian	Re	ε_c	Box	Cellular	Gaussian
4	0.50	1.6565	2.3086	2.7145	4	0.41	1.8307	2.6265	2.9386
4	0.60	1.7802	2.4051	2.5942	50	0.41	1.4129	1.8869	2.0699
4	0.70	1.4565	2.0398	2.5301	500	0.41	1.9730	2.7697	3.0613

TABLE 1. Optimal correction factor (a/ℓ) for different Re and ε_c for various kernels.

the homogeneous porous region also holds throughout the interface layer. A multiplicative correction factor to the classical permeability models can then be obtained as

$$K_{\text{model,corr}}^{-1} = K_{\text{model}}^{-1} \frac{\langle u_\gamma \rangle}{\langle u_\gamma \rangle_B}. \quad (3.5)$$

The parameter a/ℓ was tuned via a gradient-based optimization, minimizing the L^2 error between the filtered drag force and the corrected model. Figure 5(b) shows a reasonably good match between the predicted drag force with the corrected model and the filtered force. Table 1 shows the exponent parameter a/ℓ for four different porosities at $Re = 4$ and three different Reynolds numbers for $\varepsilon_c = 0.41$ using the box, cellular, and Gaussian filters. The values of a/ℓ are sensitive to the type of filter used. However, for a given filter, they do not vary significantly, suggesting that an average value for the parameter can provide good drag predictions over a range of bed porosities and Reynolds numbers.

4. Conclusions

Explicit filtering of PR-DNS data on flow over a randomly packed, monodispersed, spherical particle bed at different bed porosities and Reynolds numbers is conducted to evaluate the drag force closure model based on the Ergun equation in a volume filtered-formulation. Volume filtering across the fluid-particle interface results in a diffuse-interface, variable-porosity, single-domain approach with unit porosity in the free stream that decreases sharply in the interface region to a close-pack value within the bed. The closure model works well in the homogeneous porosity region but overpredicts the drag in the fluid-particle interface region. A uniform filter width proportional to the particle size is found to incorrectly sample large values from the free stream, resulting in significantly higher drag in the interface region. A variable filter width bounded by a unit Lipschitz constant that is proportional to the grid size in the free stream, increases in the interface region, and reaches a constant value proportional to the particle size inside the bed is devised to obtain better representation of the velocity in the bed while avoiding non-physical oscillations in porosity and permeability. To further improve the drag model, a correction scheme is developed by assuming an exponential Brinkman velocity in the interface region with an exponent as a parameter, which is tuned via a gradient-based optimization to minimize the L^2 error between the filtered DNS force and the model prediction. The correction scheme together with the variable filter width predict the drag force in the interface reasonably accurately. The tuning parameter depends on the filter kernel but has minimal sensitivity to different porosities and Reynolds numbers.

Variable filter width in the interface region may cause commutation errors. The commutation errors are estimated to be a small percentage of the total drag force; however, future work will focus on detailed quantification of these errors and the use of commutative filters to reduce them. Finally, *a posteriori* prediction solving the volume filtered equations with the corrected drag model will be performed.

Acknowledgments

The authors are extremely grateful to Drs. M. Khanwale, S. Jain, and J. Wang for hosting this project. D.F. and S.V.A. acknowledge funding from the U.S. Department of Energy's Office of Basic Energy Sciences (Geosciences) under DE-SC0021626. Discussions with Dr. X. He from the Pacific Northwest National Laboratory were invaluable. All computations were performed on Frontera computing resources under NSF's Leadership Resources Allocation.

REFERENCES

- APTE, S. V., MARTIN, M. & PATANKAR, N. A. 2009 A numerical method for fully resolved simulation (FRS) of rigid particle-flow interactions in complex flows. *J. Comput. Phys.* **228**, 2712–2738.
- BREUGEM, W., BOERSMA, B. & UITTENBOGAARD, R. 2006 The influence of wall permeability on turbulent channel flow. *J. Fluid Mech.* **562**, 35.
- BREUGEM, W.-P. 2005 The influence of wall permeability on laminar and turbulent flows. PhD thesis, Delft University of Technology.
- GERMANO, M., PIOMELLI, U., MOIN, P. & CABOT, W. H. 1991 A dynamic subgrid-scale eddy viscosity model. *Phys. Fluids A-Fluid* **3**, 1760–1765.
- HESTER, E. T., CARDENAS, M. B., HAGGERTY, R. & APTE, S. V. 2017 The importance and challenge of hyporheic mixing. *Water Resour. Res.* **53**, 3565–3575.
- KARRA, S. K., APTE, S. V., HE, X. & SCHEIBE, T. D. 2023 Pore-resolved investigation of turbulent open channel flow over a randomly packed permeable sediment bed. *J. Fluid Mech.* **971**, A23.
- MACDONALD, I., EL-SAYED, M., MOW, K. & DULLIEN, F. 1979 Flow through porous media—the Ergun equation revisited. *Ind. Eng. Chem.* **18**, 199–208.
- OCHOA-TAPIA, J. A. & WHITAKER, S. 1995a Momentum transfer at the boundary between a porous medium and a homogeneous fluid—I. Theoretical development. *Int. J. Heat Mass Tran.* **38**, 2635–2646.
- OCHOA-TAPIA, J. A. & WHITAKER, S. 1995b Momentum transfer at the boundary between a porous medium and a homogeneous fluid—II. Comparison with experiment. *Int. J. Heat Mass Tran.* **38**, 2647–2656.
- POKRAJAC, D. & DE LEMOS, M. 2015 Spatial averaging over a variable volume and its application to boundary-layer flows over permeable walls. *J. Hydraul. Eng.* **141**, 04014087.
- ROSTI, M. E., CORTELEZZI, L. & QUADRIO, M. 2015 Direct numerical simulation of turbulent channel flow over porous walls. *J. Fluid Mech.* **784**, 396–442.
- SADOWSKI, W. & DI MARE, F. 2023 Investigation of the porous drag and permeability at the porous-fluid interface: Influence of the filtering parameters on Darcy closure. *Particuology* **78**, 122–135.
- WHITAKER, S. 1996 The Forchheimer equation: a theoretical development. *Transport. Porous Med.* **25**, 27–61.